Metrology to support therapeutic and diagnostic techniques based on electromagnetics and nanomagnetics

Metrology to support therapeutic and diagnostic techniques based on electromagnetics and nanomagnetics

Gabriele Barrera, Michele Borsero, Oriano Bottauscio, Federica Celegato, Mario Chiampi, Marco Coïsson, Domenico Giordano, Massimo Inguscio, Alessandra Manzin, Enrico Simonetto, Paola Tiberto, Luca Zilberti

Abstract This paper presents an overview of the recent research activities carried on at INRIM in the field of metrology for healthcare, aiming at supporting therapeutic and diagnostic techniques based on electromagnetics and nanomagnetics. Attention is here specifically focused on three research topics, respectively related to electromagnetic dosimetry for MR-safety, production and characterization of magnetic $Ni_{80}Fe_{20}$ nanodisks for biomedical applications and development of modelling tools to support the design of novel biosensors.

Keywords Magnetic Resonance Imaging, Dosimetry, Magnetic nanoparticles, Biosensors.

1. Introduction

Diagnostic and therapeutic techniques based on electromagnetic fields and nanomagnetics are under wide development in recent years, so giving an extraordinary technological support to novel applications for healthcare.

Among the diagnostic techniques, Magnetic Resonance Imaging (MRI) has become an indispensable medical imaging modality, with about 100 million patient exams per year worldwide. The effectiveness of this technique has been largely demonstrated, being its adjustable contrast capabilities, particularly with respect to soft tissue, unmatched and not be provided by any other imaging modality. Although an excellent history of safe use, some common technical issues concerning patients' and operators' safety, as well as the possibility of extending its application, are still open, requiring the availability of reliable dosimetric studies. A significant issue is related to tissue heating by absorbed radio-frequency (RF) power (described by the Specific Absorption Rate (SAR)), in view of the use of "ultrahigh fields" MRI scanners, operating at fields greater than 7 T and consequently to higher RF frequencies. Temperature hot spots within the patient's body can arise and this emphasizes the need for local SAR control. Moreover, an estimated 8 – 10% of the European population carrying medical implants are at present excluded from receiving an MRI scan, since no metrics exists to assess the specific safety risks related to these implants.

The use of magnetic nanoparticles (MNPs) as contrast agents for enhanced imaging is strictly connected with MRI diagnosis. In addition, due to their unique properties, MNPs can become a versatile tool in a variety of biomedical applications, from targeted drug delivery to induced hyperthermia and biosensing. All these potential applications require the development of reliable methods of analysis, including experimental characterization and advanced modeling.

An overview of the ongoing research activities at the Istituto Nazionale di Ricerca Metrologica (INRIM) in Italy on the topics mentioned above is the subject of this article. The paper is subdivided into three main sections, respectively devoted to the computational and experimental dosimetry for MR-safety (Section 2), the studies on iron-nickel nanodisks for future biomedical

This contribution is the written, peer-reviewed version of a paper presented at one of the two conferences "From Life to Life: Through New Materials and Plasmonics" - Accademia Nazionale dei Lincei in Rome on June 23, 2014, and "NanoPlasm 2014: New Frontiers in Plasmonics and NanoOptics" - Cetraro (CS) on June 16-20, 2014.

Michele Borsero, Oriano Bottauscio, Marco Coïsson, Domenico Giordano, Massimo Inguscio, Alessandra Manzin, Enrico Simonetto, Paola Tiberto, Luca Zilberti
Istituto Nazionale di Ricerca Metrologica
10135 Torino, Italy
e-mail: o.bottauscio@inrim.it

Mario Chiampi
Dipartimento Energia, Politecnico di Torino
10129 Torino, Italy

Gabriele Barrera
Istituto Nazionale di Ricerca Metrologica, 10135 Torino, Italy, and
Dip. Chimica Università di Torino, 10125 Torino, Italy

applications (Section 3), and the modeling support for the development of new classes of nanostructured magnetic field sensors for MNPs detection, based respectively on Hall effect and magnetic domain wall control (Section 4).

2. Electromagnetic dosimetry for MR-safety

This section presents the computational approaches, developed at INRIM, for the prediction of the interaction between the MR electromagnetic fields (static, switched-gradient and RF fields) and human body tissues. These tools are applied to highly detailed anatomical models of human bodies, made nowadays available for a variety of human morphologies. Validation was performed by experiments using suitable phantoms, which mimic the average electromagnetic properties of human tissues, radiated by RF fields similar to the one generated by surface MR antennas. Examples of dosimetric analyses are finally given, considering three exposure scenarios: (*a*) human head exposure to the RF field generated by a 7 T bird-cage coil, (*b*) heating of metallic hip prosthesis due to the switching gradient field (GC) of a 3 T scanner in a patient's carrying bilateral implant, (c) motion induced field in a body moving around the bore of a 3 T scanner.

2.1 Computational MR dosimetry and validation

The use of ultrahigh field MR scanners and the potential extension of MR diagnostic to patients carrying implants require an accurate control of the local energy deposition (namely the Specific Absorption Rate, SAR) into tissues to avoid excessive heating. Since local SAR estimation by invasive measurements within the human body is not feasible, computational codes based on the solution of Maxwell's equations are commonly adopted to predict local distributions of electromagnetic fields and SAR. The diffusion of these tools is a direct consequence of the rapid development of new numerical algorithms combined with relatively low cost powerful computational resources (e.g. Graphic Processing Units), as well as the availability of more and more sophisticated numerical anatomical human models (Collins et al 2011, Powell et al 2012, Voigt et al 2012, Wilkoff et al 2013, Cabot et al 2013).

A computational tool, specific for MR dosimetry, has been recently developed at INRIM. The code adopts a frequency domain solver based on the T-ϕ formulation (Biro et al 1993, Krakowski 1991) for the computation of induced currents and energy deposition in a human body model. Temperature increase is consequently estimated by solving Pennes' bioheat equation (Pennes 1948). Electromagnetic and thermal problems are solved by coupling the finite element method (FEM), for handling the anatomical human body voxel structure, and the Boundary Element Method (BEM) to prevent the domain truncation and the meshing of the air and field sources. Details of the FEM-BEM model can be found in Bottauscio et al 2014.

The use of computational tools for MRI dosimetry calls for methods and procedures capable of testing the reliability of simulations, avoiding inaccuracies and pitfalls (see for example Collins et al 2003 and Zelinski et al 2008). To this end, a laboratory set-up has been worked out at INRIM (Giordano et al. 2014) and an extended comparison between simulations and measurements of radiofrequency (RF) electromagnetic near-field distributions in phantoms with tissue-simulating liquids was developed. General overall discrepancy up to 30% was found between modeling predictions and measurements, for both the electric (*E*) and magnetic (*H*) fields. Fig. 1 shows an example of the comparison between simulations using different computational tools (CST-MSW and SEMCAD software, FEM-BEM code) and experiments.

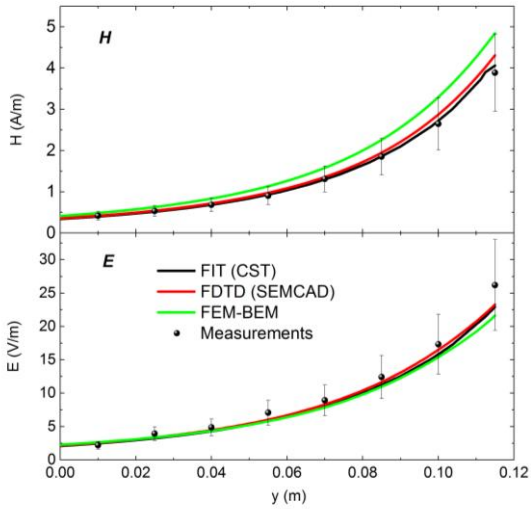

Fig.1. Comparison between measurements and simulations obtained with different computational tools (CST-MSW and SEMCAD software, FEM-BEM code). Results are compared along a radial line within the phantom radiated at 128 MHz. A coverage factor k = 2 has been associated to the measurement uncertainties.

2.2 Local SAR and temperature increment due to RF field

The evaluation of local SAR and the correlation between its spatial distribution and the temperature increment in a human body is of great relevance for MR safety. The use of dosimetric simulations is needed in presence of highly non-uniform spatial deposition of RF energy, like that produced by ultrahigh field

scanners. In the example here reported, the phenomena induced in a human head caused by the RF field of a 7 T scanner (RF frequency of 300 MHz) are simulated. The head of the Duke model (3 mm-resolution), belonging to the Virtual Family (Hasgall et al 2013, IT'IS Foundation Virtual Family dataset 2014), is radiated by a bird-cage coil, generating a 1 μT B_1^+ field in the isocenter. Local SAR and steady-state temperature increment θ in the sagittal section are shown in Fig. 2. Thermal phenomena within human body is highly affected by the perfusion coefficient (relatively low in the neck region, as shown in Fig. 2b), so that a weak spatial correlation between maximum local SAR values and temperature increments is found.

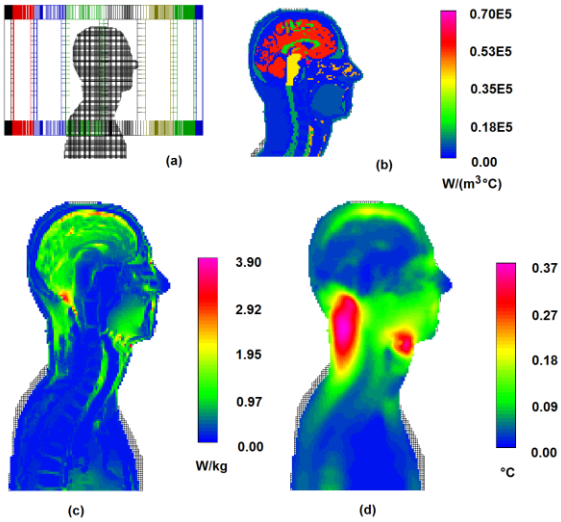

Fig.2. Local SAR and steady-state temperature increment in the sagittal section of the head model radiated by a 300 MHz bird-cage coil: (a) head/coil positioning, (b) spatial distribution of tissue perfusion coefficient, (c) local SAR distribution, (d) temperature increment.

2.3 Heating of metallic implant due to GC field

The monitoring of patients carrying orthopedic implants is one of the most promising applications of Magnetic Resonance Imaging (MRI). Nevertheless, the estimation of the dosimetric effects due to the presence of metallic prostheses is still an open issue (Schaefers et al. 2005, Stenschke et al. 2007, Mohsin et al. 2009, Powell et al. 2012, Zilberti et al 2014). In the following we summarize a study of the impact of a hip implant, exposed to the magnetic field generated by 30 mT/m conventional gradient coils driven at 1 kHz. A modified version of the Duke model has been adopted for the analysis. The voxel model of resolution 2×2×2 mm^3 was segmented into 77 tissue types and hip prostheses 168 mm long and with a 24 mm diameter femoral head were inserted into the skeletal structure to simulate a bilateral implant. Two materials were compared: Ti-6Al-4V and CoCrMo alloys with electrical and thermal conductivities of $5.8 \cdot 10^5$ Sm^{-1} and 7.2 $Wm^{-1}°C^{-1}$ and $1.16 \cdot 10^6$ Sm^{-1} and 14 $Wm^{-1}°C^{-1}$, respectively. Considering that a strong dependency of the patient/implant positioning is found, Fig. 3 shows the maximum steady-state temperature increment in proximity of the implants when the three axes gradient coils are excited and a 20% duty cycle is adopted. The increase associated with Ti6Al4V prostheses is ~60% than the one found for CoCrMo prostheses (Sanchez-Lopez et al. 2014).

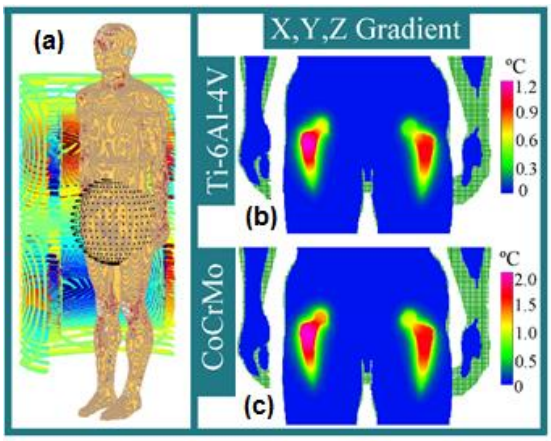

Fig.3. On the left the modified Duke model within the three gradient coils and the scanning region covering the phantom hips (a). On the right, the temperature increment in a coronal section due to the combined fields of *x*, *y* and *z* gradient coils for Ti-6Al-4V (b) and CoCrMo (c) implants.

2.4 Motion induced field

A motion-induced electric field may take place in both patients' and operators' bodies, which moves through the quite high stray stationary field of a MRI scanner. The most common biological effects associated to such field are vertigo, nausea, magnetophosphenes, metallic taste in the mouth and peripheral nerve stimulation. There is also experimental evidence of neurocognitive effects (e.g. changes in concentration). All these effects are annoying and may impair working ability. For this reason, the International Commission on Non-Ionizing Radiation Protection (ICNIRP) has published specific safety guidelines (ICNIRP 2014), including exposure limits in terms of maximum change of the magnetic flux density vector over any 3 s period and peak of the induced electric field. In order to check these exposure indexes, a potential-based formulation, written in the co-moving reference frame of the body and implemented according to the Finite Element Method, has been developed at INRIM and exploited to simulate a number of realistic exposure situations. Figure 4 shows an example of result, obtained by

simulating the Duke model moving towards the bore of a tubular 3 T scanner along the axial direction (1 m translation in 1 s, including accelerating/decelerating phases and a maximum speed of 1.2 m/s). A scheme of the trajectory is given in the inset, whereas, in the main picture, the voxels where the limit for the electric field has been exceeded are filled with a red color. Focusing the attention on the head, some points of the grey matter are not compliant with the ICNIRP Guidelines. On the contrary, concerning the variation of the flux density vector, the limit is not exceeded in the head, but only in the chest.

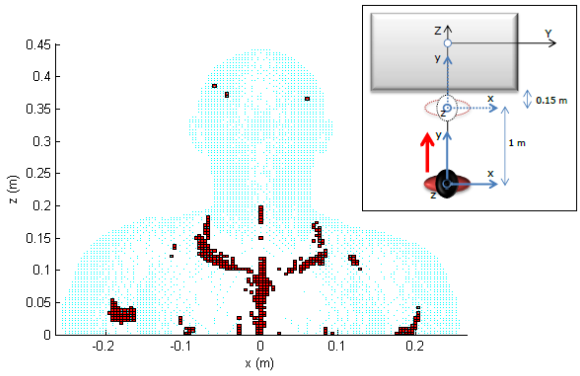

Fig.4. Motion-induced electric field for a longitudinal translation towards the bore of a 3 T scanner (1 m in 1 s, with non uniform speed). The main picture indicates the locations where the exposure index exceeds the limits for the electric field. The inset shows the path of the motion.

3. $Ni_{80}Fe_{20}$ nanodisks for biomedical applications

In this section we present a novel nanofabrication technique, developed at INRIM, based on self-assembling of polystyrene nanospheres and aimed at obtaining magnetic nanodisks suspended in ethanol. Free-standing $Ni_{80}Fe_{20}$ disks having lateral dimension of ~650 nm and thickness 30 nm were obtained by using the lithography process explained in subsection 3.1. The method turned out to be particularly attractive for being not expensive, fast over a very wide area (up to mm^2) and easy to use with respect to conventional nanolithography technique (either optical or electron) (Tiberto et al. 2010). Its major disadvantage, mainly represented by the lack of long-range order, is overcome by the detachment process and subsequent dispersion in a liquid.

The process end-product can be used as suitable magnetic carriers having nearly monodispersed size and simultaneously displaying high saturation magnetization and low-coercivity. In addition, another remarkable advantage is represented by the possibility of directly depositing by sputtering on nanodisks surface during the synthesis process.

The magnetization reversal process of $Ni_{80}Fe_{20}$ samples has been shown to be a vortex nucleation/annihilation (Novosad et al. 2005). This feature, together with the high saturation magnetisation and a low-coercivity values, represents a remarkable advantage that added to the ones of the nanofabrication process may give nanodisks a major role for bio-oriented applications (Kim et el. 2010).

3.1 Experiments

Nanodisks of $Ni_{80}Fe_{20}$ having mean diameter of ~650 nm have been designed by exploiting polystyrene nanospheres (PN) lithography. The multi-step process to obtain nanodisks is sketched in Fig. 5. To each scheme, a SEM image (FEI Inspect - F) showing the corresponding sample morphology is associated. The first step consists in depositing a continuous $Ni_{80}Fe_{20}$ thin film having thickness 30 nm by RF sputtering on a layer of optical resist (AZ5214E, thickness around 1 µm) previously spinned on a Si substrate (Fig. 5a). Secondly, a monolayer of commercially available nanospheres (starting diameter 800 nm) is deposited by floating on the film surface (Fig. 5b): the nanospheres, dispersed in a acqueous solution containing ethanol, are dropped onto $Ni_{80}Fe_{20}$ film surface and during the self-assembling solvent evaporation occurs. As can be seen, the PNs result to be substantially monodispersed and arranged in a hexagonal lattice. In the third step, the spheres diameter is reduced by plasma etching in Ar+ (Fig. 5c) in order to physically separate PNs. The SEM image shows how the self-assembly process naturally produces defects in the nanospheres array (i.e. vacancies and dislocations). Subsequently, the remaining magnetic material among the nanospheres is removed by sputter-etching (Fig. 5d). The removal of the spheres is then performed by sonication in deionized water (Fig. 5e). In order to optimize the resist removal among the spheres and overcome the reticulation process an O_2 plasma etching is performed. The corresponding tilted SEM image shows the nanodisks lying on the resist layer. The last process step, consisting in dissolving the resist layer in aceton, results in the free-standing nanodisks (Fig. 5f) that are subsequently dispersed in ethanol. A single nanodisk having a diameter around 650 nm is shown in the corresponding SEM image.

The morphology and the magnetic domain patterns of dot arrays before being detached from the substrate (stage Fig. 5e) were investigated by a conventional atomic/magnetic force microscopy (AFM/MFM), used in intermittent contact lift mode and equipped with a commercial ferromagnetic CoCr tip (MESP, coercive field ≈ 31.8 kA/m). The evolution of the magnetic domain configuration in this sample was studied by

MFM under the application of an in-plane magnetic field, generated by an electromagnet, with values up to 11.9 kA/m.

Isothermal hysteresis loops of nanopatterned films (stage Fig. 5e) were performed in the temperature interval 10÷300 K by means of an ultra-sensitive alternating-gradient field magnetometer (AGFM) operating in the field range $-1.4\cdot10^6$ A/m < H < $1.4\cdot10^6$ A/m and equipped with a liquid-He continuous flow cryostat.

Instead, the isothermal magnetization loop of free standing nanodisks in ethanol suspension was measured at room temperature by a Lakeshore Vibrating-Sample Magnetometer (VSM) operating in the magnetic field range $-1.35\cdot10^6$ A/m < H < $1.35\cdot10^6$ A/m (stage Fig. 5f).

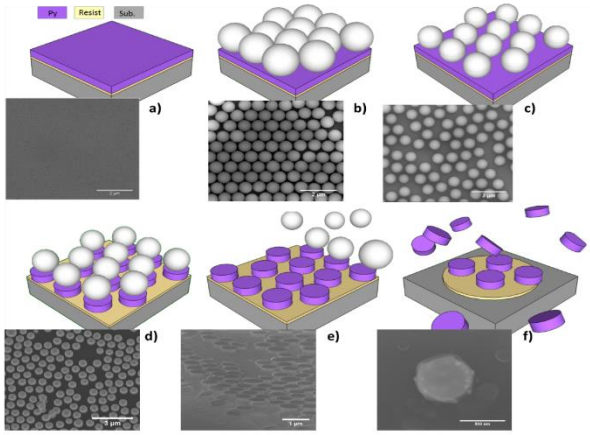

Fig. 5. Schematic description of the nanofabrication process together with corresponding SEM images: a) sputter deposition of a $Ni_{80}Fe_{20}$ layer (thickness 30 nm); b) deposition of a monolayer of polystyrene nanosphere (starting diameter 800 nm); c) Plasma etching in Ar to reduce PN diameter; d) sputter etching to remove magnetic layer among spheres; e) spheres removal by sonication; f) chemical dissolution of resist underlayer resulting in disks detachment from the substrate.

3.2 Results and discussion

Room-temperature hysteresis loops of samples at selected stages of the nanofabrication process sketched in Fig. 5 are reported in Figure 6. Curve a) corresponds to the continuous $Ni_{80}Fe_{20}$ thin film and shows the typical soft magnetic behavior with a low-field magnetization jump to reach saturation and a faint value of magnetic coercivity (stage 5a in Fig. 5). Patterned samples are generally characterized by enhanced values of both coercive field and remanence with respect to the corresponding continuous film. Hysteresis loops become wider because of shape anisotropy induced by the patterning process. In our case, the magnetization curve of dot arrays obtained by self-assembling is reported (curve e, corresponding to stage 5e of Fig. 5). It is well assessed that, depending on the aspect ratio of the magnetic dots, the magnetization behavior varies from a vortex type to a multidomains one (Novosad et al. 2001). In our case, the shape of the hysteresis loop shows a magnetization reversal typical of nucleation, displacement and annihilation of a magnetic vortex (Novosad et al. 2001). After reaching saturation, on decreasing magnetic field, a significant change of slope marking the vortex nucleation is observed. A nearly zero magnetization remanence value together with a low value of Hc (≈ 2 kA/m) are measured, the latter to be ascribed to shape anisotropy. Finally, field magnetization behavior of free-standing nanodisks after being dispersed in ethanol is reported in curve f (sample corresponding to stage 5f of Figure 5). No substantial difference with the magnetization reversal shown for dot arrays attached on a substrate is observed, being typical of vortex nucleation/annihilation for both systems. However, a much lower, non-zero, value of coercivity is observed (≈ 716 A/m) pointing to the desirable magnetic properties for exploitation in biomedical applications (Rozhkova et al. 2009).

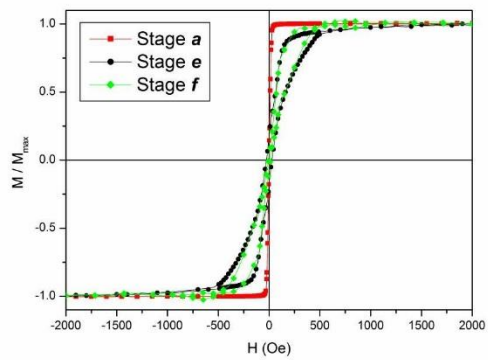

Fig. 6. Room-temperature hysteresis loops of selected samples corresponding to different stages of the nanofabrication process: a) continuous Ni80Fe20 thin film (stage 1a, Figure 1); e) $Ni_{80}Fe_{20}$ dot arrays (stage 5e, Figure 5); f) free standing $Ni_{80}Fe_{20}$ nanodisks dispersed in ethanol (stage 5f, Figure 5).

An AFM image of arrays of dots prepared by self-assembling (stage 5e in Figure 5) of polystyrene nanospheres having initial diameter 800 nm together with the corresponding MFM image acquired at magnetization remanence after applying a magnetic field perpendicular to the film plane of about 795 kA/m are reported in Fig. 7. The topographical image confirms the regular assembling of the PNs that form an hexagonal lattice whose regularity strictly depends on intrinsic properties of the assembling process. Brighter spots may be ascribed to some polymer remaining on the top of nanostructures. As it can be observed in the MFM image, the magnetization reversal is dominated by a vortex process as indicated

by the presence of a magnetic vortex in almost every dot, evidenced by the darker circular region marking the vortex core (see as an example the dots in the dashed circle). Such an observation is in full agreement with the hysteresis loop behavior reported in Fig. 6. Moreover, all vortex cores show the same contrast, indicating that the magnetization in each dot has the same perpendicular direction. Such a behavior can be ascribed to film magnetic history with a final remanent state coming from a saturated one obtained with a magnetic field applied perpendicularly to the film plane. Conversely, the solid circle marks a sample region in which the self-assembling process fails to create well separated nanostructures. In this case, the corresponding magnetic domains arrangement results to be not a vortex-like but multidomain, typical of a continuous $Ni_{80}Fe_{20}$ thin film.

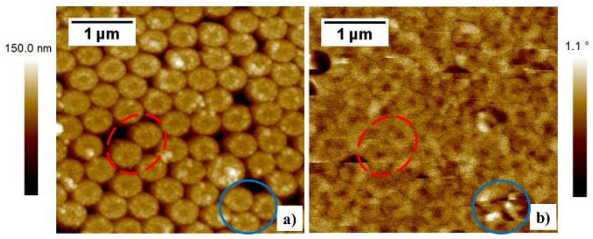

Fig. 7. a) AFM image of $Ni_{80}Fe_{20}$ dot array (lateral dimension 650 nm, thickness 30 nm) by self-assembling (stage 5e in Figure 5) of polystyrene nanospheres; b) corresponding MFM image acquired at magnetisation remanence after applying a magnetic field perpendicular to the film plane of ~795 kA/m. Circles indicate different regions on the film surface.

4. Modelling of nanostructured magnetic field sensors

In the last decade, the advances in nanostructure fabrication have given a boost to the development of novel magnetic sensors for metrological applications in biology and medicine, such as the detection of functionalized magnetic labels for biomolecular targeting, drug delivery, sample purification and cell manipulation. In the landscape of magnetic biosensor technologies, Hall effect and magnetoresistance based devices offer promising properties in terms of high sensitivity, magnetic field resolution, easy miniaturization and lab-on-chip integration (Llandro et al. 2010; Tamanaha et al. 2008). However, their development and use in biomolecular recognition and single molecule detection still remain a challenging task.

A valid support to the design and optimization of high-sensitivity elements can be provided by *ad-hoc* numerical models, able to simulate the specific physical phenomena involved in the magnetic field detection mechanism. For example, several studies have been focused on the calculation of the electric potential distribution in semiconductor Hall probes under non-uniform magnetic fields, by adopting classical models of the Hall effect in the diffusive transport regime (Folks et al. 2009; Manzin et al. 2012). At the same time, advanced micromagnetic models have been implemented to investigate the magnetization state, induced by external magnetic fields, of magnetoresistive sensing elements, e.g. giant magnetoresistance (GMR) multilayers, spin-valves, magnetic tunnel junction (MTJ) devices and anisotropic magnetoresistance (AMR) nanostructures (Freitas et al. 2007).

In this scenario, the fundamental role of numerical modeling is here demonstrated for two applications recently investigated at INRIM in the framework of the EMRP Project IND08 *"Metrology for advanced industrial magnetics - MetMags"*. The attention has been focused on miniaturized Hall devices made of graphene and AMR sensing elements based on domain wall control, for possible use in the detection of magnetic micro/nano-beads (ensembles of superparamagnetic nanoparticles embedded in polymer micro/nano-spheres).

4.1 Modelling of graphene Hall effect based sensors

The high room temperature carrier mobility, robustness to large biasing currents and low-cost production make graphene a promising material for high-sensitivity Hall elements, in alternative to semiconductor heterostructures (Huang et al. 2014; Xu et al. 2013; Tang et al. 2011). Depending on graphene fabrication process (chemical vapor deposition, thermal sublimation of SiC or exfoliation), different device performances are expected, requiring an accurate characterization of electronic transport properties (Panchal et al. 2014) and a high-resolution sensitivity mapping. The latter can be achieved by using scanning gate microscopy techniques, where magnetically coated tips are employed to map the sensor response to localized magnetic fields. Despite the high resolution, a correct interpretation of the experimental results requires a clear separation of magnetic and parasitic electric field contributions. In particular, the tip-sample capacitive coupling can lead to a local modification of the carrier density, strongly perturbing the measured Hall signal.

As recently demonstrated (Rajkumar et al. 2013), numerical modeling is a powerful tool for the interpretation of scanning gate microscopy images on graphene, which results to be particularly reactive to tip-induced electric fields. This is well illustrated by Fig. 8, which reports the calculated maps of the transverse voltage for a micron sized Hall cross made of epitaxial graphene grown on SiC (intrinsically n-

doped), when including (left) and neglecting (right) tip-sample capacitive coupling. In presence of electric field effects, caused by an unbalance between the potentials on the tip and in the device region beneath the tip, a two-fold symmetry is observed, with peak values at the corners of the active sensing area and a non-zero signal at the cross center. When reversing the current direction, the two-fold symmetry rotates such that the voltage polarity flips everywhere. As confirmed by the map calculated when excluding electrical interaction, the signal at the cross center results from the Lorentz force due to the tip magnetic stray field. Conversely, the peak values are a consequence of the tip-sample capacitive coupling, which leads to an accumulation or depletion of charges in the graphene region underneath the tip.

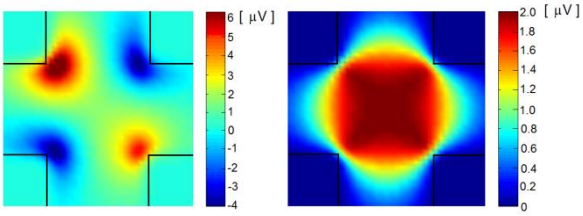

Fig. 8 Simulated maps of the transverse voltage for a micron sized Hall cross made of epitaxial graphene with carrier density of 7.5×10^{11} cm^{-2} and mobility of 1000 cm^2/Vs. In the *left picture*, tip-sample capacitive coupling is included, while in the *right picture* it is excluded. A zero lift height with respect to the sensor surface is considered.

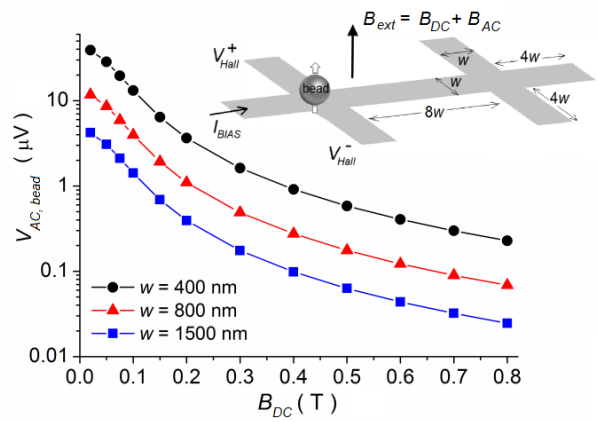

Fig. 9 Calculated amplitude of the AC Hall voltage due to a micro-bead placed in contact with the surface of an epitaxial graphene Hall sensor, as a function of B_{DC} and device width w (I_{bias} = 75 μA). The inset shows the scheme of the considered Hall bars, with the bead at the cross center. The graphene sample has a carrier density of 2×10^{12} cm^{-2} and a mobility of 3000 cm^2/Vs.

An accurate mapping of graphene device sensitivity to localized magnetic fields requires the elimination of electric field perturbing effects. This can be experimentally achieved by implementing a Kelvin probe feedback loop in the standard scanning gate microscopy setup (Rajkumar et al. 2014). Such characterization is fundamental for the device optimization and successive application in the detection of magnetic bio-labels.

Recently, it has been demonstrated that miniaturized Hall crosses made of epitaxial graphene can be employed as sensors of beads with micrometer size (Panchal et al. 2013; Manzin et al. 2015). As for conventional semiconductor devices, the bead detection and susceptibility mapping can be performed by using an AC-DC Hall magnetometry technique (Mihajlović et al. 2007). A uniform external field, composed of a DC and a small AC signals (B_{ext} = B_{DC}+B_{AC}), is applied perpendicularly to the sensor surface. The bead presence leads to a change in the amplitude of the in-phase component of the AC response, which is proportional to the variation in the bead magnetic susceptibility. As an example, Fig. 9 shows the amplitude of the calculated AC Hall voltage ($V_{AC,bead}$) as a function of B_{DC}, when a bead comprised of iron oxide nanoparticles embedded into a polystyrene sphere with 1 μm diameter (Dynal, MyOne) is placed above the active area of an epitaxial graphene device. The curves are computed for different values of cross width w, ranging from to 0.4 μm to 1.5 μm.

The non-linearity of the bead magnetization curve, which saturates at ~0.8 T, leads to a rapid reduction in $V_{AC,bead}$ with the DC field increase, following the bead susceptibility decay. For the entire interval of B_{DC}, the sensitivity reduces by a factor of ~9 when increasing the device width up to 1.5 μm. Larger signals are generally observed in comparison to InSb devices thanks to the possibility of applying high bias currents. However, the performances of graphene sensors can deteriorate in presence of defects and heterogeneities, e.g. multi-layer islands and topographic corrugations. Hence, only a proper selection of experimental parameters (sensor width, supply mode and DC field for bead magnetization) can guarantee high detectable signals (Manzin et al. 2015).

4.2 Modelling of magnetic domain wall based sensors

Another class of magnetic field sensors for potential use in magnetic label detection is represented by magnetoresistive devices based on domain wall (DW) control. Typical geometries for DW confinement are represented by nanowires with artificial constrictions or pinning sites, like notches or corners (O'Brien et al. 2011).

Recently, it has been demonstrated that permalloy nanowires with L-shaped (Fig. 10a) or zig-zag structure can be adopted for detecting the low magnetic field produced by micro-beads (Donolato et al. 2009; Huang et al. 2013; Corte-León et al. 2015). For certain amplitudes and orientations of the external field, the magnetization configuration at the nanostructure corner can be characterized by the presence of a transverse

DW. This magnetic domain state is illustrated in Fig. 10a, which reports the magnetization spatial distribution calculated at remanence for a 150 nm width device after sweeping the external field from negative saturation to zero along an angular orientation β = 10˚. If a magnetized bead is located in proximity to the device corner, it produces a stray field that interacts with the DW, modifying the energy landscape and thus possibly causing a shift in the depinning field required to move the DW.

The DW pinning/depinning behavior can be monitored via magnetoresistance measurements by exploiting the AMR effect. This phenomenon, which derives from the anisotropic scattering of conduction electrons due to spin-orbit interaction, leads to a local dependence of electrical conductivity on the mutual orientation of magnetization **M** and current density **J**. In particular, the conductivity is maximal (minimal) when vectors **M** and **J** are locally orthogonal (parallel).

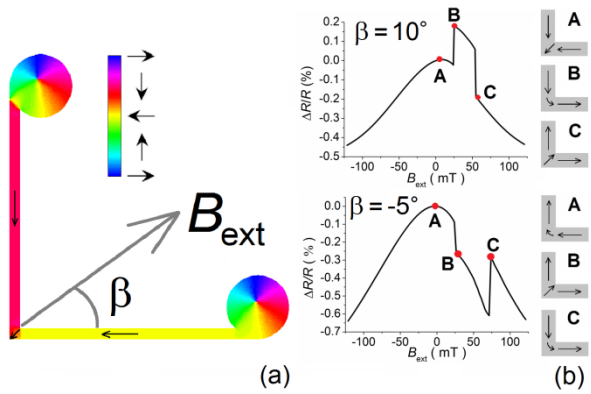

Fig. 10 a) Simulated magnetization state at remanence for a permalloy L-shaped nanowire with width of 150 nm and thickness of 25 nm, after sweeping the external field from negative saturation to zero along an angular orientation β = 10˚. The color scale identifies the magnetization angle (in degrees) with respect to *x*-axis. b) Calculated AMR response of the same device for a field applied at an angle β of 10˚ (*top*) and -5˚ (*bottom*). *On the right*: schematic magnetic configurations at the equilibrium points depicted in the graphs.

The L-shaped nanowire depicted in Fig. 10a generally exhibits a magnetoresistance response characterized by two irreversible jumps, corresponding to the non-synchronous switching of the magnetization in the two arms (Manzin et al. 2014; Corte-León et al. 2014). Depending on the field orientation, the two switching events occur in different order (Fig. 10b). For positive field orientation the remanent state is characterized by DW confinement at the device corner, followed by DW depinning (resistance increase) and then by DW pinning (resistance decrease). For negative field orientation no DW is present at the corner at remanence and the first switching event is characterized by DW pinning, followed by DW depinning. The role of circular disks at the arm ends in promoting DW pinning/depinning phenomena is put in evidence in Fig. 10a, which shows the creation of vortex state in the disks at remanence.

The formation and annihilation of DWs are also influenced by the nanowire width *w* (see Fig. 11), as a result of the arm shape anisotropy, i.e., the strong geometric anisotropy of narrower arms leads to a higher coercivity and thus to higher switching fields. When a micro-bead is placed over the device corner, a modification of the magnetoresistive response can be observed, depending on sensor width and field angular orientation. It has been demonstrated that the presence of a Dynal bead with 1 μm diameter can be detected only when employing devices with *w* lower than 200 nm (strong bead-DW interaction) and applying fields with negative angular orientation. In this case, a zero variation in the pinning field is observed, while an increase in the depinning one, with a maximum change of ~10 mT, is numerically estimated, as a proof of the bead presence (Corte-León et al. 2015).

Further studies are in progress to improve the device sensitivity, aiming at increasing the bead-induced variation in the DW depinning field and reducing the impact of stochastic processes on the device magnetization reversal that is at the base of the sensing mechanism.

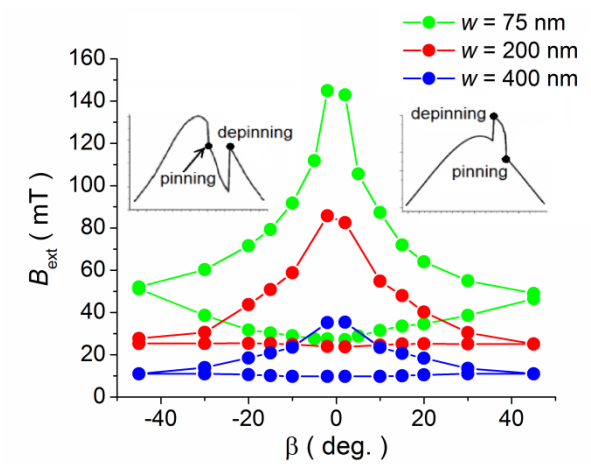

Fig. 11 (a) Calculated DW pinning and depinning fields versus angular orientation of the external field β for permalloy L-shaped nanostructures with variable width *w*.

Acknowledgments The research activities here described were developed under two Joint Research Projects (JRP) of the European Metrology Research Programme: EMRP-HLT06 “Metrology for next-generation safety standards and equipment in MRI” (2012–2015) and EMRP-IND08 "Metrology for advanced industrial magnetics – MetMags” (2011–2014). EMRP is jointly funded by the EMRP participating countries within EURAMET and the European Union.

Funding was also received from the Italian MIUR project P7 “Metrology for therapeutic and diagnostic techniques based

on electromagnetic radiation and ultrasound waves" (2014-2016).

References

Biro O, Preis K, Renhart W, Vrisk G, Richter KR (1993) Computation of 3-D current driven skin effect problems using a current vector potential. IEEE Trans. Magn., 29, 2: 1325-1328.

Bottauscio O, Chiampi M, and Zilberti L (2014) Massively parallelized Boundary Element simulation of voxel-based human models exposed to MRI fields, IEEE Trans. Magn. 50, 2 (7025504).

Cabot E, Lloyd T, Christ A, Kainz W, and Douglas M (2013) Evaluation of the RF heating of a generic deep brain stimulator exposed in 1.5 T magnetic resonance scanners. Bioelectromagnetics, 34, 2: 104-113.

Collins CM, and Smith MB (2003) Spatial resolution of numerical models of man and calculated Specific Absorption Rate using the FDTD Method: A study at 64 MHz in a Magnetic Resonance Imaging coil- J. Magn. Reson. Imaging 18: 383–388.

Collins CM, and Wang Z (2011) Calculation of radiofrequency electromagnetic fields and their effects in MRI of human subjects. Magn. Reson. Med. 65: 1470–1482.

Corte-León H, Krzysteczko P, Schumacher HW, Manzin A, Antonov V, Kazakova O (2015) Magnetic bead detection using domain wall-based nanosensor. J Appl Phys (in print)

Corte-León H, Nabaei V, Manzin A, Fletcher J, Krzysteczko P, Schumacher HW, Kazakova O (2014) Anisotropic magnetoresistance state space of permalloy nanowires with domain wall pinning geometry. Scientific Reports 4(6045)

Donolato M et al (2009) Nanosized corners for trapping and detecting magnetic nanoparticles. Nanotechnology 20(385501)

Folks L et al (2009) Near-surface nanoscale InAs Hall cross sensitivity to localized magnetic and electric fields. J Phys: Condens Matter 21(255802).

Freitas PP, Ferreira R, Cardoso S, Cardoso F (2007) Magnetoresistive sensors. J. Phys.: Condens Matter 19(165221)

Giordano D, Zilberti L, Borsero M, Chiampi M, Bottauscio O (2014) Experimental validation of MRI dosimetric simulations in phantoms including metallic objects. IEEE Trans. Magn. 50, 11 (5101504).

Huang L, Zhang Z, Chen B, Ma X, Zhong H, Peng LM (2014) Ultra-sensitive graphene Hall elements. Appl Phys Lett 104(183106).

Huang HT, Ger TR, Lin YH, Wei ZH (2013) Single cell detection using a magnetic zigzag nanowire biosensor. Lab Chip 13:3098-3104

Hasgall PA, Neufeld E, Gosselin MC, Klingenböck A, Kuster N (2013) IT'IS Database for thermal and electromagnetic parameters of biological tissues. Version 2.3, February 11th, 2013. www.itis.ethz.ch/database.

Kim DH, Rozhkova EA, Ulasov IV, Bader SD, Rajh T, Lesniak MS, Novosad V (2010) Biofunctionalized magnetic vortex microdisks for targeted cancer cell destruction. Nature Materials, 9: 165-171.

Krakowski MR (1991) Some theorems of the eddy-current theory. Archiv für Elektrotechnik, 74: 329-334.

International Commission on non-Ionizing Radiation Protection (2014), Guidelines for limiting exposure to electric fields induced by movement of the human body in a static magnetic field and by time-varying magnetic fields below 1 Hz. Health Physics 106, 3: 418-425.

IT'IS Foundation Virtual family dataset 2014, http://www.itis.ethz.ch/news-events/news/latest-news/.

Llandro J, Palfreyman JJ, Ionescu A, Barnes CHV (2010) Magnetic biosensor technologies for medical applications: a review. Med Biol Eng Comput 48:977–998.

Manzin A, Nabaei V, Kazakova O (2012) Modelling and optimization of submicron Hall sensors for the detection of superparamagnetic beads. J Appl Phys 111(07E513).

Manzin A, Simonetto E, Amato G, Panchal V, Kazakova O (2015) Modeling of graphene Hall effect sensors for microbead detection. J Appl Phys (in print).

Manzin A, Nabaei V, Corte-León H, Kazakova O, Krzysteczko P, Schumacher HW (2014) Modeling of anisotropic magnetoresistance properties of permalloy nanostructures. IEEE Trans Magn 50(7100204)

Mohsin SA , Sheikh NM, Abbas W (2009) MRI induced heating of artificial bone implants. J. Electromagnet. Wave. 23: 799-808.

Novosad V, Fradin FY, Roy PE, Buchanan K, Guslienko KY, Bader SD (2005) Magnetic Vortex Resonance in Patterned Ferromagnetic Dots. Phys. Rev. B 72(024455).

Novosad V, Guslienko KY, Shima H, Otani Y, Fukamichi K, Kikuchi N, Kitakami O, Shimada Y (2001) Nucleation and annihilation of magnetic vortices in submicron ferromagnetic dots. IEEE Trans. Magn. 374: 2088-2090.

O'Brien L et al (2011) Tunable remote pinning of domain walls in magnetic nanowires. Physical Review Letters 106, (087204)

Panchal V, Lartsev A, Manzin A, Yakimova R, Tzalenchuk A, Kazakova O (2014) Visualisation of edge effects in side-gated graphene nanodevices. Scientific Reports 4(5881).

Pennes HH (1948) Analysis of tissue and arterial blood temperatures in the resting human forearm. Journal of Applied Physiology, 1:93–122.

Powell J, Papadaki A, Hand J, Hart A, and McRobbie D (2012) Numerical simulation of SAR induced around Co-Cr-Mo hip prostheses in situ exposed to RF Fields associated with 1.5 and 3 T MRI body coils. Magn. Reson. Med 68: 960–968.

Rajkumar RK, Manzin A, Cox DC, Silva SRP, Tzalenchuk A, Kazakova O (2013) 3-D mapping of sensitivity of graphene Hall devices to local magnetic and electrical fields. IEEE Trans Magn 49: 3445-3448.

Rajkumar RK, Asenjo A, Panchal V, Manzin A, Iglesias-Freire O, Kazakova O (2014) Magnetic scanning gate microscopy of graphene Hall devices. J. Appl. Phys. 115(172606).

Rozhkova EA, Novosad V, Kim DH, Pearson J, Divan R, Rajh T, Bader SD (2009) Ferromagnetic microdisks as carriers for biomedical application. J. Appl. Phys., 105(07B306).

Sanchez-Lopez H, Zilberti L, Bottauscio O, Hand J, Papadaki A, Tang F, Chiampi M, Crozier S (2014) Heating of bilateral hip prostheses in a human body model induced by a multi-axis gradient coil set, Proc. Joint Annual Meeting ISMRM, Milan (Italy), May 2014, ISSN 1545-4428: 4878.

Schaefers G, and Kugel H (2005) A basic investigation of heating effects on total hip prostheses in combination with a simulated skin contact of the inner thighs during magnetic resonance imaging (MRI) with an 1.5 Tesla MR system. Proc ISMRM Workshop on MRI Safety: Update, Practical Information and Future Implications, McClean, Virginia, USA.

Stenschke J, Li D, Thomann M, Schaefers G, and Zylka W (2007) A numerical investigation of RF heating effect on implants during MRI compared to experimental measurements. Adv. Med. Eng. 114(pt 1): 53–58.

Tamanaha CR, Mulvaney SP, Rife JC, Whitman LJ (2008) Magnetic labeling, detection, and system integration. Biosensors and Bioelectronics 24:1–13.

Tang CC, Li MY, Li LJ, Chi CC, Chen JC (2011) Characteristics of a sensitive micro-Hall probe fabricated on chemical vapor deposited graphene over the temperature range from liquid-helium to room temperature. Appl Phys Lett 99(112107).

Tiberto P, Boarino L, Celegato F, De Leo N, Coïsson M, Vinai F, Allia P (2010) Magnetic and magnetotransport properties of arrays of nanostructured antidots obtained by self-assembling polystyrene nanosphere lithography. J. Appl. Phys., 107(09B502).

Voigt T, Homann H, Katscher U, and Doessel O (2012) Patient-individual local SAR determination: in vivo measurements and numerical validation. Magn. Reson. Medicine, 68, 4: 1117-1126.

Wilkoff BL, Albert T, Lazebnik M, Park S_M, Edmonson J, et al. (2013) Safe magnetic resonance imaging scanning of patients with cardiac rhythm devices: A role for computer modeling. Heart Rhythm 10, 12: 1815-1821.

Xu H, Zhang Z, Shi R, Liu H, Wang Z, Wang S, Peng LM (2013) Batch-fabricated high-performance graphene Hall elements. Scientific Reports 3(1207).

Zelinski AC, Goyal VK, Adalsteinsson E, Wald LL (2008) Fast, accurate calculation of maximum local N-gram Specific Absorption Rate. Proc. Intl. Soc. Mag. Reson. Med. 16 (1188).

Zilberti L, Bottauscio O, Chiampi M, Hand J, Sanchez Lopez H, Crozier S (2014) Collateral thermal effect of MRI-LINAC gradient coils on metallic hip prostheses. IEEE Trans. Magn. 50, 11 (5101704).